

## Article

# A General Parameter Optimization Method for a Capacitive Power Transfer System with an Asymmetrical Structure

Jinglin Xia <sup>1</sup>, Xinmei Yuan <sup>1</sup> , Sizhao Lu <sup>2</sup>, Weiju Dai <sup>3</sup>, Tong Li <sup>2</sup>, Jun Li <sup>1</sup> and Siqi Li <sup>2,\*</sup>

<sup>1</sup> State Key Laboratory of Automotive Simulation and Control, Jilin University, Changchun 130025, China; xiajl18@mails.jlu.edu.cn (J.X.); yuan@jlu.edu.cn (X.Y.); junli610@263.net (J.L.)

<sup>2</sup> Department of Electrical Engineering, Kunming University of Science and Technology, Kunming 650500, China; lusz10@kust.edu.cn (S.L.); 20192205006@stu.kust.edu.cn (T.L.)

<sup>3</sup> CSG Electric Power Research Institute of Yunnan Power Grid Corporation, Kunming 650106, China; dwj0479@163.com

\* Correspondence: lisiqi@kust.edu.cn

**Abstract:** Capacitive power transfer (CPT) is an attractive wireless power transfer (WPT) technology and it has been widely studied in many applications. Symmetrical structures and high-order compensation networks are always produced as optimization results and common configurations for high-efficiency CPT systems. However, in space-limited scenarios, an asymmetric structure tends to be a better choice. The related large number of high-order asymmetric system parameters is a key problem in parameter design. In this study, a general parameter design method that is based on reactive power optimization is proposed for an electric field resonance-based CPT system with an asymmetric six-plate coupler. The reactive power in the compensation network was analyzed and optimized under the constraint of transferred power. With equal reactive power, the optimization complexity was significantly reduced and the optimized system parameters were provided. To validate the effectiveness of the proposed method, a 1 MHz, 3.2 kW asymmetric CPT prototype with 100 mm gap distance was implemented. The results indicate that, with the optimized parameters, high system efficiency can be achieved when the system's volume is reduced. At the rated power, about 95% DC–DC overall efficiency was achieved through a 6-pF coupling capacitor.

**Keywords:** general parameter design; asymmetrical coupler structure; reactive power optimization; electric field resonance (EFR); capacitive power transfer (CPT)



**Citation:** Xia, J.; Yuan, X.; Lu, S.; Dai, W.; Li, T.; Li, J.; Li, S. A General Parameter Optimization Method for a Capacitive Power Transfer System with an Asymmetrical Structure. *Electronics* **2022**, *11*, 922. <https://doi.org/10.3390/electronics11060922>

Academic Editors: Qi Zhu and Aiguo Patrick Hu

Received: 18 February 2022

Accepted: 14 March 2022

Published: 16 March 2022

**Publisher's Note:** MDPI stays neutral with regard to jurisdictional claims in published maps and institutional affiliations.



**Copyright:** © 2022 by the authors. Licensee MDPI, Basel, Switzerland. This article is an open access article distributed under the terms and conditions of the Creative Commons Attribution (CC BY) license (<https://creativecommons.org/licenses/by/4.0/>).

## 1. Introduction

Wireless power transfer (WPT) technology that offers a way to transfer electric power through air or other another nonconductive medium has more advantages than traditional conductive charging technology [1–3]. In recent years, WPT technologies have been widely studied and many commercialized products have been released in low-power and high-power applications [4–7], such as consumer electronics [8–11], electrical machines [12–14], biomedical devices [15–19], and transportation systems [20–25]. Among the WPT technologies, inductive power transfer (IPT) and capacitive power transfer (CPT) are the two main types in which a magnetic field or an electric field is utilized for power transmission, respectively.

Inductive wireless power transfer is one of the most promising WPT technologies and extensive studies have been implemented on the IPT system. In the IPT system, the magnetic coupler is a key component that always consists of transmission coils with a symmetric or asymmetric structure [26]. Since the magnetic couplers are always loosely coupled [27], heavy ferrite cores are needed in order to redistribute the magnetic field in the coupler and enhance the magnetic coupling of the transmission coils. Besides this, shielding plates are required to prevent the magnetic field from leaking into the surrounding environment. To improve the transferred power and efficiency, compensation

circuits are needed in order to achieve circuit resonance. The basic compensation circuit topology is just one resonant capacitor that is connected in series or parallel with each of the transmission coils [28–30]. The high-order compensation circuit's topology consists of a complex circuit structure, such as inductance–capacitance–capacitance (LCC) [31,32], inductance–capacitance–inductance (LCL) [33], series–series–parallel (S-SP) [34,35], or series–parallel–series (SP-S) [36]. With more freedom within their parameter design than in those of a basic compensation circuit, high-order compensation circuits can achieve zero-voltage switching (ZVS), zero phase angle (ZPA), and a constant current/voltage (CC/CV) output at the same time with appropriate parameter design [37,38]. Within compensation circuits, the transferred power of IPT systems can be up to ten kilowatts (kW) under a transmission distance of hundreds of mm and the transmission efficiency can be up to 90–96% [31,39]. However, due to the eddy current effect, the magnetic field in the coupler can cause a huge temperature rise in the surrounding metal objects, which threatens the operation of the system [40]. In contrast, the electric field in the capacitive coupler, which is used for power transmission in CPT systems, does not cause a significant temperature rise in metal objects [41]. Besides this, the capacitive coupler always consists of several metal plates. Compared with the expensive and heavy ferrite cores that are found in IPT systems, the cost and weight of the CPT system can be reduced. Therefore, the CPT system is becoming an attractive alternative for the IPT system and an increasing amount of research is focused on CPT technologies, recently [5].

In the literature regarding CPT systems, most of the research focuses on the design of the capacitive coupler and compensation circuit [5]. The capacitive coupler in the CPT system is always made up of several metal plates with a rectangular or circular shape. The coupling structure can be configured in a rotating [42], horizontal [25,43], vertical [44], or interleaved style [45]. Generally, there are at least four plates in the capacitive coupler, two of which are set as transmitting plates and the other two plates are set as receiving plates. The mutual capacitances are generated between the transmitting plates and receiving plates. In order to improve the transferred power and efficiency, the compensation circuits are needed to make the circuit resonant, which allows it to achieve zero phase angle (ZPA) on the grid side [40]. Just like the IPT system, the basic compensation circuit of the CPT system is just one inductor connected in series or parallel with the capacitive coupler at the transmitting side and receiving side [46,47], respectively. However, in long-distance applications, the mutual capacitance of the coupler is very small (usually in the range of several to tens of picofarads), which makes the compensation inductors very large (usually in the range of several millihenry). To further improve the transferred power and reduce the value of the compensation inductors, a high frequency and high-order compensation circuit is needed [40]. Nowadays, the operating frequency of a CPT system is usually in the range of several or tens of megahertz (MHz). High-order compensation circuits, such as LCL [44,48], electric field resonance (EFR) [49,50], capacitance–inductance–inductance–capacitance (CLLC) [51], multistage LC [52,53], and inductance–capacitance–inductance–capacitance (LCLC) [25,40] compensation circuits, provide large voltage gains and improve the capability of power transmission. With these compensation circuits, the transferred power of the CPT system can be up to several kW and the transmission distance can be up to hundreds of mm; the system's performance is significantly improved. In [25,40], a double-sided LCLC compensation circuit was used for a horizontal four-plate coupler, about 1.5 kW of power was transferred through a 150 mm transmission distance with a DC–DC overall efficiency of 93.5% [40]. However, the coupling plate voltage can be up to several kilovolts, which may be excessive of the safety limit, causing electromagnetic radiation (EMR) problems and serious security incidents. As a solution, shielding structures were added to the traditional four-plate coupler and a six-plate coupler was proposed in [48,49]. With the shielding plates covering over the capacitive coupler, the electric field emission can be significantly reduced. Besides this, the parasitic capacitance of the shielding plates can also be used as the resonant capacitance, which can eliminate the external capacitance of the compensation circuit, such as makes the LCLC compensation circuit into a LCL

compensation circuit [44]. In [49], a six-plate coupler-based EFR compensation circuit was proposed and about 91.1% DC–DC overall efficiency was achieved with a transferred power of 700 W. However, high-order compensation circuits increase the total number of circuit parameters. A large number of circuit parameters make it difficult to design and optimize the system's parameters. To optimize the circuit's parameters and improve the system's efficiency, Lagrange multipliers and two-stage optimization methods were proposed in [50,53–56]. In [53–56], the multistage LC matching networks were analyzed by using the method of Lagrange multipliers and the number of matching network stages and the distribution of the gains and compensation among the stages were optimized in order to achieve high-efficiency matching networks. Reference [50] proposes a two-stage parameter design method for an EFR-based CPT system, which can optimize the system parameters through optimizing the reactive power in the coupling capacitor  $C_5$  and the whole system. With the proposed two-stage method, when 3 kW of power is transferred over a distance that is under 100 mm, the system efficiency can be up to 95.7%. According to the optimization results in [50,53–56], the optimized CPT systems tend to have symmetric circuit parameters when the compensation circuits on the primary side and secondary side are the same. The coupling structures of the capacitive coupler are also symmetric. However, in many practical applications, especially for mobile devices [57], unmanned aerial vehicles [58,59], and electric vehicles (EVs) wireless charging applications [60,61], the available installation space on the receiving side is always smaller than that which is available on the transmitting side, which limits the volume of the receiver. In these scenarios, the receiver needs to be compact and flat. An asymmetric coupler structure is an effective configuration for the WPT systems that are used in these applications [59]. The asymmetric coupler structure leads to asymmetric system parameters. The optimization results from symmetric cases are not suitable for a system with asymmetric parameters and the use of systematic parameter optimization methods for asymmetric CPT systems is rarely mentioned in previous studies.

In this present study, an EFR-based six-plate capacitive coupler with an asymmetric structure was used in order to make an asymmetric CPT system for EV wireless charging applications. A general parameter optimization method that is based on reactive power optimization is proposed for this asymmetric CPT system. A capacitive coupler with different geometry was analyzed and modeled. According to the circuit model, the appropriate voltage and current were obtained in order to derive the system's reactive power. Under the constraint of transferred power, the reactive power was optimized based on the independence of the circuit parameters. By using equal reactive power, the general circuit conditions under which the circuit parameters should be satisfied were derived. With these circuit conditions, the optimization complexity was reduced and the optimized asymmetric system parameters were given.

The following is the organization of this paper. Section 2 introduces the asymmetric coupling structure and the modeling of the asymmetric CPT system. Based on this circuit model, the system's reactive power and its effect on the system's efficiency are derived. Section 3 analyzes the independence of the circuit parameters and proposes a general parameter optimization method. Section 4 introduces the implementation of this method. The effectiveness of the proposed method is verified in Section 5. Section 6 provides the conclusions.

## 2. Modelling of the CPT System

### 2.1. Asymmetrical Capacitive Coupler Model

A capacitive coupler that consists of six rectangular metal plates was used in this experiment. The typical structure is shown in Figure 1.  $l_1$  and  $l_2$  are the plate lengths,  $d_1$ ,  $d_2$ , and  $d_{12}$  are the airgap distances. There were 15 coupling capacitors in the six-plate coupler and the performance of this structure can be characterized by four primary capacitors,  $C_{S1}$ ,  $C_{S2}$ ,  $C_2$ , and  $C_3$ .  $C_{S1}$  and  $C_{S2}$  represent the equivalent mutual capacitors between the transmitting plates and receiving plates;  $C_2$  and  $C_3$  represent the equivalent self-capacitors

between the transmitting plates or between the receiving plates. The equivalent circuit model with four coupling capacitors is shown in Figure 2a [48]. Due to the fact that the capacitors  $C_{S1}$  and  $C_{S2}$  are connected in series, the coupling capacitor  $C_S$  can be further simplified, where

$$C_S = \frac{C_{S1} \cdot C_{S2}}{C_{S1} + C_{S2}} \tag{1}$$

As described in [50], a symmetric CPT system with an identical transmitter and receiver is verified to be an efficient configuration. However, the shielding distances  $d_1$  and  $d_2$  tend to have large values (usually in the range of 50 mm to 100 mm) in order to achieve high system efficiency. For space-limited scenarios, such as EV wireless charging applications, the limited space in the receiving side determines that the shielding distance  $d_2$  cannot be very large. Therefore, an asymmetric coupler with different distances  $d_1$  and  $d_2$  (where  $d_1 > d_2$ ) is more practical in EV wireless charging applications. According to the different plate lengths  $l_1$  and  $l_2$ , the asymmetric structure can be divided into three categories:  $l_1 = l_2$ ,  $l_1 > l_2$ , and  $l_1 < l_2$ , as shown in Figure 3.

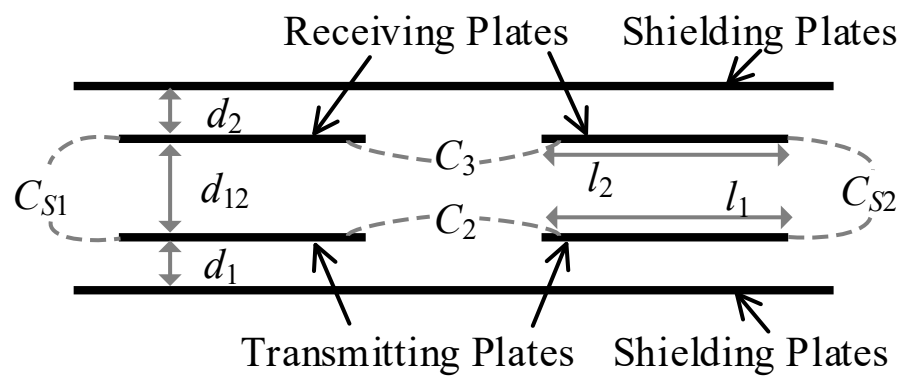


Figure 1. Typical configuration of a capacitive coupler with six plates.

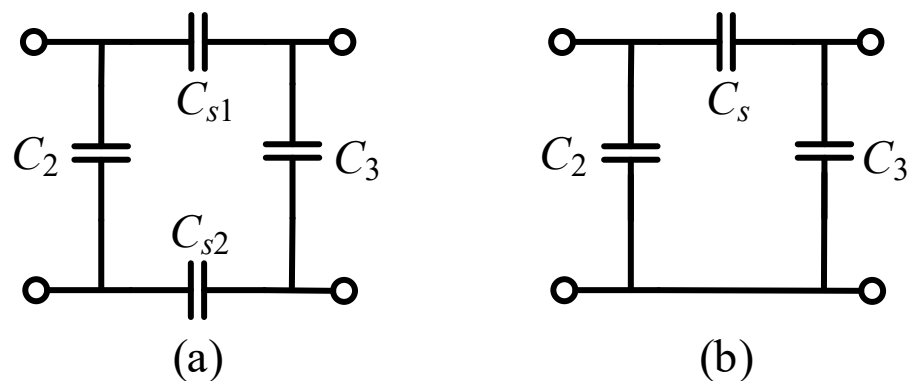


Figure 2. Modelling of the capacitive coupler. (a) with four coupling capacitors. (b) with three coupling capacitors.

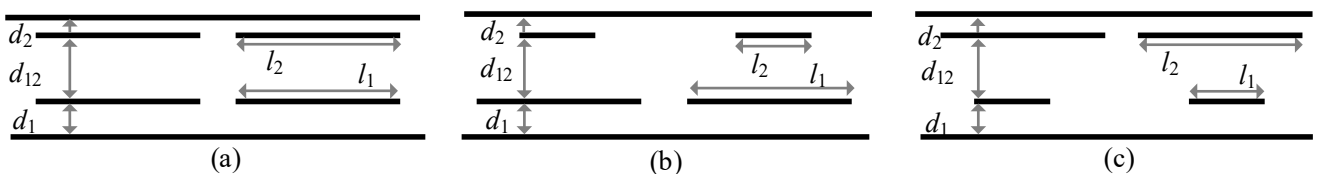


Figure 3. Asymmetric structures of a six-plate coupler. (a)  $l_1 = l_2$ ,  $d_1 > d_2$ . (b)  $l_1 > l_2$ ,  $d_1 > d_2$ . (c)  $l_1 < l_2$ ,  $d_1 > d_2$ .

In the capacitive coupler, the coupling capacitors  $C_2$ ,  $C_3$ , and  $C_5$  are determined by the airgap distances  $d_1$ ,  $d_2$ , and  $d_{12}$  and plate lengths  $l_1$  and  $l_2$ . An asymmetric coupler structure always results in asymmetric circuit parameters. In Figure 3a and c,  $l_1$  is not greater than  $l_2$  and  $d_1$  is greater than  $d_2$ , as a result the capacitor value of  $C_2$  is less than that of  $C_3$ . In Figure 3b, the relationship between  $C_2$  and  $C_3$  is determined by the asymmetric distance and plate length and the equivalent  $C_2$  and  $C_3$  can be obtained by appropriate configuration. When the plate lengths  $l_1$  and  $l_2$  are not equal, as shown in Figure 3b,c, a small horizontal misalignment has little effect on the coupling capacitance. In the cases in which  $l_1 \geq l_2$ , as shown in Figure 3a,b, the leaked electric field that results from the small misalignment conditions are mostly exposed to the receiving side. As a comparison, the leaked electric field that results from small misalignment conditions for the asymmetric coupler that is shown in Figure 3c are mostly exposed to the transmitting side. Considering this, the asymmetric structure that is shown in Figure 3c was selected in order to form the asymmetric CPT system in this study.

2.2. CPT System Model

In this study, an EFR compensation network was used. With the asymmetric capacitive coupler that is shown in Figure 3c, the equivalent circuit model of the asymmetric CPT system is shown in Figure 4, where  $C_3$  is greater than  $C_2$ . The EFR compensation circuit was formed by  $L_1$ ,  $C_1$ ,  $L_2$ ,  $C_2$ ,  $L_3$ ,  $C_3$ ,  $L_4$ , and  $C_4$ .  $M_{12}$  and  $M_{34}$  represent the mutual inductances between  $L_1$  and  $L_2$  and between  $L_3$  and  $L_4$ , respectively.  $C_5$  represents the mutual capacitance in the capacitive coupler.  $V_{in}$  and  $V_{out}$  are the input and output direct current (DC) voltage sources, respectively. The capacitors  $C_2$ ,  $C_3$ , and  $C_5$  achieve EFR in the compensation circuit and the EFR is resonant with the inductors  $L_2$  and  $L_3$  at an angular frequency of  $\omega_0$ . Besides this,  $C_1$  and  $C_4$  are resonant with  $L_1$  and  $L_4$  at an angular frequency of  $\omega_0$ , respectively.

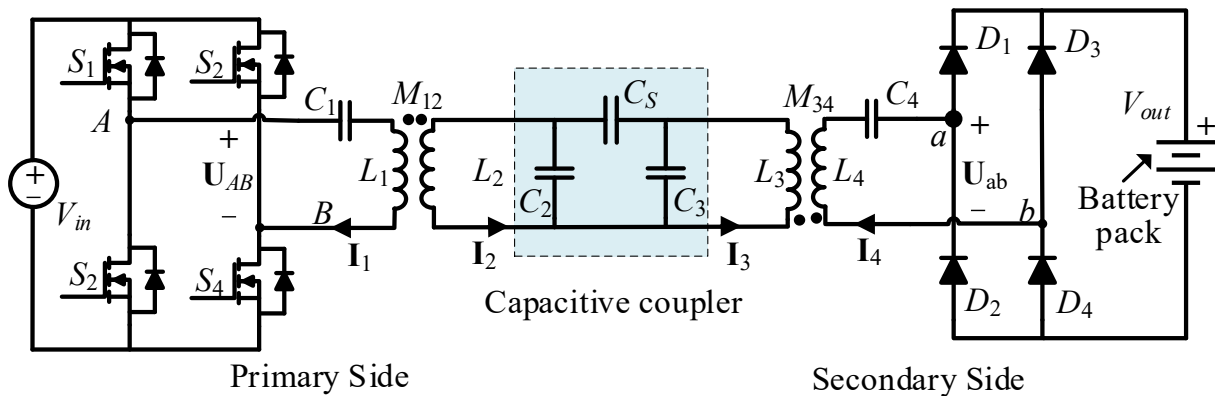


Figure 4. An EFR-based asymmetric CPT system model.

As shown in Figure 5, the equivalent circuit model of an EFR-based CPT system can be obtained according to the method of fundamental harmonics approximation. The internal resistances of all of the circuit components are ignored.  $U_{21}$ ,  $U_{12}$ ,  $U_{43}$ , and  $U_{34}$  represent the induced voltage sources that are generated in the coupling inductors  $L_1$ ,  $L_2$ ,  $L_3$ , and  $L_4$ .  $U_{AB}$  and  $U_{ab}$  represent the input and output AC voltages, respectively, where

$$\begin{cases} U_{AB} = V_{in} \cdot 2\sqrt{2}/\pi \\ U_{ab} = V_{out} \cdot 2\sqrt{2}/\pi \end{cases} \quad (2)$$

By using  $U_{AB}$  as the reference, the voltage and current phasors can then be obtained based on the superposition theorem as follows [50]:

$$\left\{ \begin{array}{l} U_{AB} = U_{AB} \angle 0^\circ = U_{AB} \\ U_{ab} = U_{ab} \angle 90^\circ = jU_{ab} \\ U_{C2} = -\frac{U_{AB}M_{34}(C_3+C_S)+U_{ab}M_{12}C_S}{\omega_0^2 M_{12}M_{34}(C_3C_S+C_2C_S+C_2C_3)} \\ U_{C3} = -\frac{U_{AB}M_{34}C_S+U_{ab}M_{12}(C_2+C_S)}{\omega_0^2 M_{12}M_{34}(C_3C_S+C_2C_S+C_2C_3)} \\ I_1 = \frac{U_{ab}C_S}{j\omega_0^3 M_{12}M_{34}(C_3C_S+C_2C_S+C_2C_3)} \\ I_2 = -\frac{jU_{AB}}{\omega_0 M_{12}} \\ I_3 = \frac{jU_{ab}}{\omega_0 M_{34}} \\ I_4 = \frac{jU_{AB}C_S}{\omega_0^3 M_{12}M_{34}(C_3C_S+C_2C_S+C_2C_3)} \end{array} \right. \quad (3)$$

We can see from Equation (3) that the current and voltage phasors on the input side are in phase, which means zero phase angle is achieved on the input side. Since all of the internal resistances are not considered, the output power is equal to the input power, which can be described as

$$P = -U_{AB}I_1 = U_{ab}I_4 = \frac{U_{AB}U_{ab}C_S}{\omega_0^3 M_{12}M_{34}(C_2C_3 + C_2C_S + C_3C_S)} \quad (4)$$

The mutual inductances  $M_{12}$  and  $M_{34}$  that are featured in Equation (4) can be described as

$$\left\{ \begin{array}{l} M_{12} = K_{12} \sqrt{\frac{1}{\omega_0^2 C_1} \frac{C_3+C_S}{\omega_0^2 (C_2C_3+C_3C_S+C_3C_S)}} \\ M_{34} = K_{34} \sqrt{\frac{1}{\omega_0^2 C_4} \frac{C_2+C_S}{\omega_0^2 (C_2C_3+C_3C_S+C_3C_S)}} \end{array} \right. \quad (5)$$

where  $K_{12}$  and  $K_{34}$  are the coupling coefficients. By substituting Equation (5) into Equation (4), the transferred power can be further described as

$$P = \frac{\omega_0 C_S U_{AB} U_{ab} \sqrt{C_1 C_4}}{K_{12} K_{34} \sqrt{(C_3 + C_S)(C_2 + C_S)}} \quad (6)$$

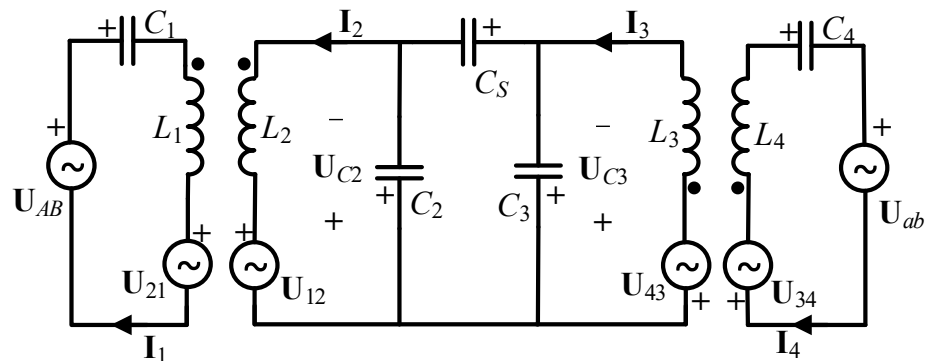


Figure 5. Equivalent circuit model of an asymmetric CPT system.

### 2.3. Reactive Power on a Compensation Network

According to Equations (3) and (5), the capacitive reactive power in the system that is shown in Figure 5 can be obtained as follows:

$$\left\{ \begin{aligned} Q_{C1} &= \frac{\omega_0 U_{ab}^2 C_4 C_5^2}{K_{12}^2 K_{34}^2 (C_3 + C_5)(C_2 + C_5)} \\ Q_{C2} &= \frac{\omega_0 K_{34}^2 U_{AB}^2 C_1 C_2 (C_3 + C_5)(C_2 + C_5)^2 + \omega_0 K_{12}^2 U_{ab}^2 C_2 C_4 (C_3 + C_5) C_5^2}{K_{12}^2 K_{34}^2 (C_2 C_3 + C_3 C_5 + C_3 C_5)(C_3 + C_5)(C_2 + C_5)} \\ Q_{C3} &= \frac{\omega_0 K_{12}^2 U_{ab}^2 C_4 (C_3 + C_5)(C_2 + C_5)^2 C_3 + \omega_0 K_{34}^2 U_{AB}^2 C_1 (C_2 + C_5) C_5^2 C_3}{K_{12}^2 K_{34}^2 (C_2 C_3 + C_3 C_5 + C_3 C_5)(C_3 + C_5)(C_2 + C_5)} \\ Q_{C4} &= \frac{\omega_0 U_{AB}^2 C_1 C_5^2}{K_{12}^2 K_{34}^2 (C_3 + C_5)(C_2 + C_5)} \\ Q_{C5} &= \frac{\omega_0 K_{34}^2 U_{AB}^2 C_1 (C_2 + C_5) C_5 C_3^2 + \omega_0 K_{12}^2 U_{ab}^2 C_4 (C_3 + C_5) C_5 C_2^2}{K_{12}^2 K_{34}^2 (C_2 C_3 + C_3 C_5 + C_3 C_5)(C_3 + C_5)(C_2 + C_5)} \end{aligned} \right. \quad (7)$$

Here,  $Q_C$  is used to represent the total capacitive reactive power, where

$$\begin{aligned} Q_C &= Q_{C5} + Q_{C1} + Q_{C2} + Q_{C3} + Q_{C4} \\ &= \omega_0 C_1 U_{AB}^2 \left( \frac{C_5^2}{K_{12}^2 K_{34}^2 (C_3 + C_5)(C_2 + C_5)} + \frac{1}{K_{12}^2} \right) + \omega_0 C_4 U_{ab}^2 \left( \frac{C_5^2}{K_{12}^2 K_{34}^2 (C_3 + C_5)(C_2 + C_5)} + \frac{1}{K_{34}^2} \right) \end{aligned} \quad (8)$$

According to Equations (3) and (5), the reactive power on inductors  $l_1, l_2, l_3,$  and  $l_4$  can be calculated as follows:

$$\left\{ \begin{aligned} Q_{L1} &= \frac{\omega_0 C_4 U_{ab}^2 C_5^2}{K_{12}^2 K_{34}^2 (C_3 + C_5)(C_2 + C_5)} \\ Q_{L2} &= \frac{\omega_0 C_1 U_{AB}^2}{K_{12}^2} \\ Q_{L3} &= \frac{\omega_0 C_4 U_{ab}^2}{K_{34}^2} \\ Q_{L4} &= \frac{\omega_0 C_1 U_{AB}^2 C_5^2}{K_{12}^2 K_{34}^2 (C_3 + C_5)(C_2 + C_5)} \end{aligned} \right. \quad (9)$$

The total inductive reactive power  $Q_L$  can be described as

$$\begin{aligned} Q_L &= Q_{L1} + Q_{L2} + Q_{L3} + Q_{L4} \\ &= \omega_0 C_1 U_{AB}^2 \left( \frac{C_5^2}{K_{12}^2 K_{34}^2 (C_3 + C_5)(C_2 + C_5)} + \frac{1}{K_{12}^2} \right) + \omega_0 C_4 U_{ab}^2 \left( \frac{C_5^2}{K_{12}^2 K_{34}^2 (C_3 + C_5)(C_2 + C_5)} + \frac{1}{K_{34}^2} \right) \end{aligned} \quad (10)$$

Since the CPT system is in a resonant state, the total capacitive reactive power and total inductive reactive power are equal. We can see from Equations (7)–(10) that the reactive power is excited by the voltage sources  $U_{AB}$  and  $U_{ab}$ . Since the expressions of the reactive power are complex, the optimization of the reactive power is very difficult.

### 2.4. Analysis of System Efficiency

The efficiency of the CPT system is determined by the transferred power and power losses in the circuit components. Increasing the transferred power while decreasing the losses can improve the transmission efficiency. Typically, the power losses are divided into four main parts: rectifier loss  $P_{loss,rec}$ , inverter loss  $P_{loss,inv}$ , capacitor loss  $P_{loss,C}$ , and inductor loss  $P_{loss,L}$ . Considering these losses, the system’s efficiency  $\eta$  can be expressed as

$$\eta = \frac{P}{P + P_{loss,rec} + P_{loss,inv} + P_{loss,C} + P_{loss,L}} \quad (11)$$

where

$$\left\{ \begin{aligned} P_{loss,C} &= \sum P_{loss,Ci} & (i = S, 1, 2, 3, 4) \\ P_{loss,L} &= \sum P_{loss,Lj} & (j = 1, 2, 3, 4) \end{aligned} \right. \quad (12)$$

In Equation (11), the rectifier loss and inverter loss include the switching losses and conduction losses, which are determined by the switching devices and switching states; the losses in the inductors and capacitors are mainly determined by the reactive power that is in the passive components and the quality factors of the components. Therefore, the applications of low conduction-resistance power devices and high quality factor passive components and the realization of a ZVS state are usually efficient methods for the CPT system [40,56]. When the switching devices and transferred power are determined, we assume that the rectifier loss and inverter loss are constants. In this case, the system efficiency can be improved by reducing the losses in the passive components.

Here, the reactive power of the passive components can be represented as  $Q_{Ci}$  and  $Q_{Lj}$ ; the quality factors can be represented as  $Q_{Ci}^*$  and  $Q_{Lj}^*$ . The power losses in the passive components can be further described as

$$\begin{cases} P_{loss,Ci} = \frac{Q_{Ci}}{Q_{Ci}^*}, & P_{loss,Lj} = \frac{Q_{Lj}}{Q_{Lj}^*} \\ P_{loss,C} = \sum \frac{Q_{Ci}}{Q_{Ci}^*}, & P_{loss,L} = \sum \frac{Q_{Lj}}{Q_{Lj}^*} \end{cases} \quad \begin{matrix} (i = S, 1, 2, 3, 4) \\ (j = 1, 2, 3, 4) \end{matrix} \quad (13)$$

The system efficiency can be obtained from Equations (11)–(13) as

$$\eta = \frac{1}{1 + \sum \frac{Q_{Ci}}{Q_{Ci}^* P} + \sum \frac{Q_{Lj}}{Q_{Lj}^* P} + \frac{P_{loss,rec} + P_{loss,inv}}{P}} \quad (i = S, 1, 2, 3, 4; j = 1, 2, 3, 4). \quad (14)$$

In this study, the inductors were wound with Litz wire and the capacitors usually had low dissipation factors. To simplify the analysis, we assumed that all of the capacitors (inductors) had the same quality factors, which can be represented as  $Q_C^*$  ( $Q_L^*$ ). Given these facts, Equation (14) can be changed to

$$\eta = \frac{1}{1 + \frac{1}{2} \left( \frac{1}{Q_C^*} + \frac{1}{Q_L^*} \right) \left( \frac{Q_C}{P} + \frac{Q_L}{P} \right) + \frac{P_{loss,rec} + P_{loss,inv}}{P}} \quad (15)$$

where  $Q_C$  and  $Q_L$  represent the total capacitive or inductive reactive power in the CPT system. When the transferred power is determined, the efficiency in Equation (15) can be improved by decreasing the reactive power or increasing the quality factors. When the quality factors are determined, the transmission efficiency is mainly dependent on the reactive power. Therefore, the reactive power in the CPT system should be optimized for efficiency improvement. The cases in which the passive components have different quality factors are described in Appendix A.

### 3. General Optimization Method

As described above, under the constraint of transferred power, the reactive power should be optimized in order to improve the system's efficiency. In this case, we set the ratio of reactive power to transferred power as the optimization objective. Based on the properties of a linear CPT system, a general optimization method was proposed in order to reduce the optimization's complexity. By applying the equal reactive power to the optimization objective, the general circuit conditions under which the circuit parameters should be satisfied were obtained. Based on the circuit conditions, the system model can be simplified and all of the system parameters can be optimized.

#### 3.1. General Optimization Method Based on Equal Reactive Power

To minimize the optimization objective, the transferred power should be considered while minimizing the reactive power. Therefore, the transferred power can be seen as a constraint for the reduction of the reactive power. Since the total inductive reactive power was equal to the total capacitive reactive power, it was sufficient to minimize the inductive reactive power in this study.

In the CPT system, the reactive power is excited by the voltage sources  $U_{AB}$  and  $U_{ab}$ , which can be represented as  $Q_{AB}$  and  $Q_{ab}$ , respectively. From Equation (10),  $Q_{AB}$  and  $Q_{ab}$  can be expressed as

$$\begin{cases} Q_{AB} = \omega_0 C_1 U_{AB}^2 \left( \frac{C_5^2}{K_{12}^2 K_{34}^2 (C_3 + C_5)(C_2 + C_5)} + \frac{1}{K_{12}^2} \right) \\ Q_{ab} = \omega_0 C_4 U_{ab}^2 \left( \frac{C_5^2}{K_{12}^2 K_{34}^2 (C_3 + C_5)(C_2 + C_5)} + \frac{1}{K_{34}^2} \right) \end{cases} \quad (16)$$

From Equations (10) and (16), the inductive reactive power can then be expressed as

$$Q_L = Q_{AB} + Q_{ab} \quad (17)$$

In this study, the system parameters  $\omega_0$ ,  $U_{AB}$ ,  $U_{ab}$ ,  $K_{12}$ ,  $K_{34}$ ,  $C_1$ ,  $C_4$ ,  $C_2$ ,  $C_3$ , and  $C_5$  are independent; they can be adjusted independently. Since the reactive powers  $Q_{AB}$  and  $Q_{ab}$  in the linear system are excited by the independent voltage sources  $U_{AB}$  and  $U_{ab}$ ,  $Q_{AB}$  and  $Q_{ab}$  are independent. The relationship between the transferred power  $P$  and the reactive power  $Q_{AB}$  and  $Q_{ab}$  can then be expressed as

$$\sqrt{Q_{AB} Q_{ab}} = P \sqrt{\left( \frac{1}{K_{34} K_{12} \sqrt{\left(\frac{C_3}{C_5} + 1\right) \left(\frac{C_2}{C_5} + 1\right)}} + \sqrt{\left(\frac{C_3}{C_5} + 1\right) \left(\frac{C_2}{C_5} + 1\right)} \right)^2 + \left(\frac{1}{K_{12}} - \frac{1}{K_{34}}\right)^2} \quad (18)$$

We can see from Equation (18) that when the transferred power is determined, the product of  $Q_{AB}$  and  $Q_{ab}$  has a minimum value. For each given product value of  $Q_{AB}$  and  $Q_{ab}$ , the total inductive reactive power has a minimum value, where

$$Q_L \geq 2\sqrt{Q_{AB} Q_{ab}} \quad (19)$$

The equal sign in Equation (18) is achieved when  $Q_{AB}$  and  $Q_{ab}$  are equal. Under the constraint of transferred power, it can be verified that equal  $Q_{AB}$  and  $Q_{ab}$  can be achieved. Here, we set the equal reactive powers  $Q_{AB}$  and  $Q_{ab}$  as a circuit condition. According to the equal reactive powers  $Q_{AB}$  and  $Q_{ab}$ , the total inductive reactive power can then be expressed as

$$\begin{aligned} Q_L &= 2\sqrt{Q_{AB} Q_{ab}} \\ &= 2\omega_0 U_{AB} U_{ab} \sqrt{C_1 C_4 \left( \frac{C_5^2}{(C_3 + C_5)(C_2 + C_5)} \frac{1}{K_{12}^2 K_{34}^2} + \frac{1}{K_{12}^2} \right) \left( \frac{C_5^2}{(C_3 + C_5)(C_2 + C_5)} \frac{1}{K_{12}^2 K_{34}^2} + \frac{1}{K_{34}^2} \right)} \end{aligned} \quad (20)$$

where

$$U_{AB}^2 C_1 \left( C_5^2 + K_{34}^2 (C_3 + C_5)(C_2 + C_5) \right) = U_{ab}^2 C_4 \left( C_5^2 + K_{12}^2 (C_3 + C_5)(C_2 + C_5) \right) \quad (21)$$

Considering the transferred power, the optimization objective can then be derived from Equations (6) and (20) as

$$\frac{Q_L}{P} = 2\sqrt{\frac{1}{K_{12}^2} + \frac{1}{K_{34}^2} + \frac{(C_2 + C_5)(C_3 + C_5)}{C_5^2} + \frac{1}{K_{12}^2 K_{34}^2} \frac{C_5^2}{(C_2 + C_5)(C_3 + C_5)}} \quad (22)$$

Furthermore, Equation (22) can be expressed as

$$\frac{Q_L}{P} = 2 \sqrt{\left( \frac{1}{K_{34}K_{12}\sqrt{\left(\frac{C_3}{C_5}+1\right)\left(\frac{C_2}{C_5}+1\right)}} + \sqrt{\left(\frac{C_3}{C_5}+1\right)\left(\frac{C_2}{C_5}+1\right)} \right)^2 + \left(\frac{1}{K_{12}} - \frac{1}{K_{34}}\right)^2} \tag{23}$$

Since  $K_{12}$  and  $K_{34}$  are independent, their values can be adjusted independently. For each given value of  $K_{12}$  and  $K_{34}$ , the optimization objective in Equation (23) can be further decreased when  $K_{12}$  and  $K_{34}$  are equal. In this case, Equation (23) can be changed to

$$\frac{Q_L}{P} = \frac{2}{K_{12}K_{34}\sqrt{\left(\frac{C_3}{C_5}+1\right)\left(\frac{C_2}{C_5}+1\right)}} + 2\sqrt{\left(\frac{C_3}{C_5}+1\right)\left(\frac{C_2}{C_5}+1\right)} \tag{24}$$

where

$$K_{12} = K_{34} \tag{25}$$

By substituting Equation (25) into Equation (21), the relationship between  $C_1$  and  $C_4$  can be obtained as

$$U_{AB}^2 C_1 = U_{ab}^2 C_4 \tag{26}$$

In this study, an asymmetric six-plate capacitive coupler was used, where  $C_2 < C_3$ . To simplify the analysis, the coefficients  $a$  and  $b$  are used to describe the relationship between capacitors  $C_2$ ,  $C_3$  and  $C_5$ , where

$$C_2 = aC_5, \quad C_3 = bC_5 \tag{27}$$

From Equations (27) and (24), the optimization objective can be derived as

$$\frac{Q_L}{P} = \frac{2}{K_{12}K_{34}\sqrt{(a+1)(b+1)}} + 2\sqrt{(a+1)(b+1)} \tag{28}$$

When the value of  $b$  is determined, the minimized  $Q_L/P$  can be obtained. At the minimum value point, the value of  $a$  can be expressed as

$$a = \frac{1}{K_{12}K_{34}(b+1)} - 1 \tag{29}$$

where

$$\min \frac{Q_L}{P} = \frac{4}{\sqrt{K_{12}K_{34}}} = \frac{4}{K_{12}} = \frac{4}{K_{34}} \tag{30}$$

We can see from Equation (30) that the minimum value of  $Q_L/P$  is just related to the coupling coefficients; by increasing the values of  $K_{12}$  and  $K_{34}$ , the value of  $Q_L/P$  can be further decreased.

By substituting Equations (25) and (26) into Equation (6), the transferred power can be described as

$$P = \frac{\omega_0 U_{AB} U_{ab} \sqrt{C_1 C_4}}{K_{12} K_{34} \sqrt{(a+1)(b+1)}} \tag{31}$$

According to Equation (2), Equation (31) can be changed to

$$P = \frac{8\omega_0 V_{in} V_{out} \sqrt{C_1 C_4}}{\pi^2 K_{12} K_{34} \sqrt{(a+1)(b+1)}} \tag{32}$$

From the above analysis, a general parameter optimization method that is based on equal reactive power can be obtained. Figure 6 shows the design flowchart. Considering the actual application scenarios, the system requirements are given and defined as inputs. The optimized coefficients  $K_{12}$ ,  $K_{34}$ ,  $a$  and  $b$  can be obtained by Equations (25), (28) and (29). Based on Equation (27), the relationship between the coupling capacitors can be derived. With the given airgap distances  $d_{12}$  and  $d_2$ , an appropriate capacitive coupler with optimized coupling capacitors can be determined. According to Equations (26) and (27), the optimized  $C_1$  and  $C_4$  can be obtained. The resonant inductors can then be obtained by using the resonant conditions. Finally, the parameters can be adjusted iteratively depending on the available commercial inductors and capacitors.

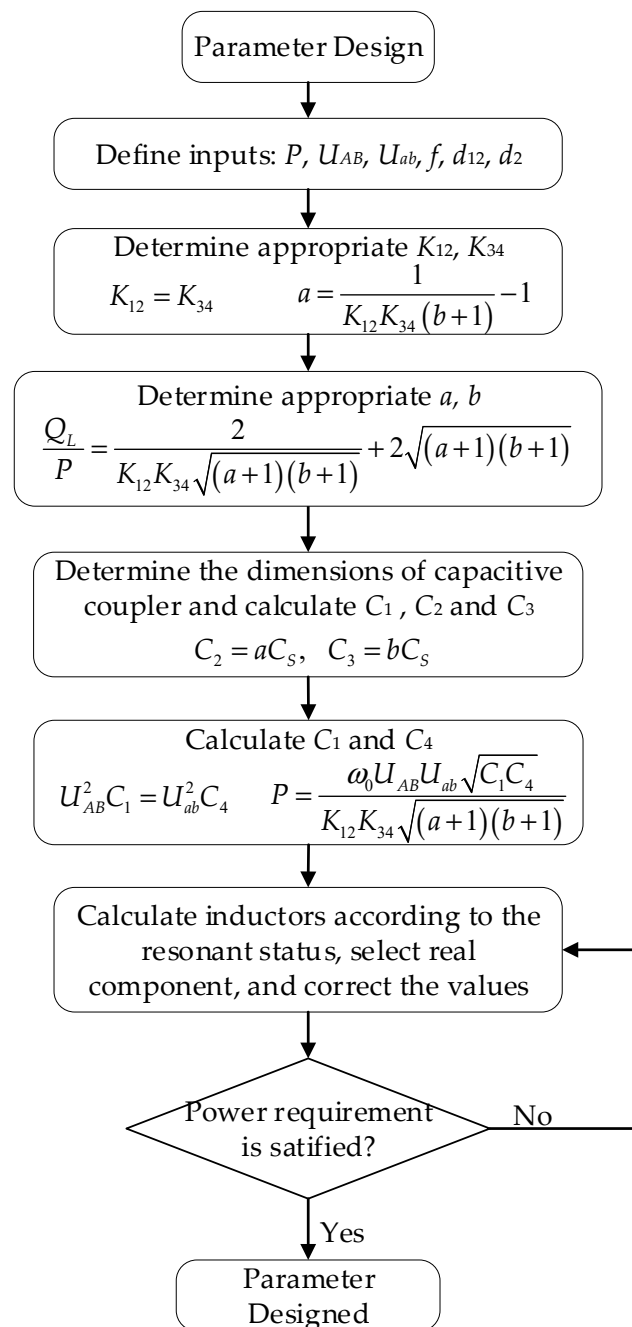


Figure 6. Parameter design flowchart.

### 3.2. Comparison with the General Optimization Method

Both the two-stage optimization method [50] and the general optimization method that is proposed in this study aim to increase the system's efficiency by optimizing the reactive power in the CPT system. The optimization objectives and optimization processes in the two methods are similar. The difference is that in the two-stage optimization method the capacitive coupler is first optimized and then the symmetric coupling parameters are verified to be an efficient configuration for the CPT system. The two-stage method is suitable for a CPT system with symmetric circuit parameters. In order to further the research, this paper studies the asymmetric CPT system and its general optimization method. Based on the properties of a linear CPT system, equal reactive power was used to optimize the reactive power in the CPT system. This method is suitable for both symmetric and asymmetric CPT systems. Besides this, when the coupling capacitors  $C_2$  and  $C_3$  were equal, the optimization results in the two studies were same.

## 4. Parameter Design and Implementation

Considering the actual requirements in EV wireless charging applications, a CPT prototype with an asymmetric coupling structure was implemented in order to validate the proposed method.

### 4.1. System Requirements

As shown in Table 1, the system requirements in an actual CPT system are given. To satisfy the requirements of the charging distance and passability, the transferred distance  $d_{12}$  was set to 100 mm. Since the installation space under the vehicle chassis was limited, the airgap distance  $d_2$  on the vehicle's side was set to 20 mm. The operating frequency of the CPT system was 1 MHz. The transferred power was set to 3.2 kW and both the input and output voltages were set to 450 V.

**Table 1.** System requirements.

Designator	Description	Designed Values
$d_{12}$	Transferred distance	100 mm
$d_2$	Airgap distance	20 mm
$f$	Resonant frequency	1 MHz
$P$	Transferred power	3200 W
$V_{out}$	Output DC voltage	450 V
$V_{in}$	Input DC voltage	450 V
$K_{12}, K_{34}$	Coupling coefficient	0.4

We can see from Equations (28) and (30) that the optimization objective can be reduced by increasing the value of the coupling coefficients  $K_{12}$  and  $K_{34}$ . However, studies have shown that a large third harmonic can be induced in the inverter when  $K_{12}$  and  $K_{34}$  are greater than 0.4 [62]. Therefore, the values of  $K_{12}$  and  $K_{34}$  were both set to 0.4 in this study.

### 4.2. Coupler Design

In this study, the asymmetric six-plate capacitive coupler was formed by 2 mm-thick aluminum plates. The structure is shown in Figure 7 and the dimensions of the designed coupler are shown in Table 2. The transmitting plates and receiving plates are square and centrosymmetric. On the receiving side, the plate length  $l_2$  was 600 mm, the shielding edges  $l_{e3}$  and  $l_{e4}$  were both 50 mm, and the plate separation  $l_{s2}$  was 100 mm. The distance  $d_2$  was 20 mm and the transmission distance  $d_{12}$  was 100 mm. The remaining dimensions of the transmitting side were plate length  $l_1$  and distance  $d_1$ .

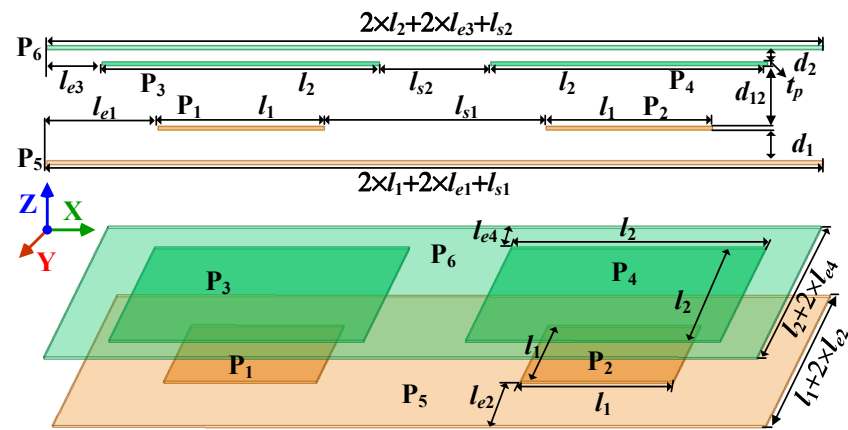


Figure 7. Structure and dimensions of the asymmetric six-plate coupler.

Table 2. Dimensions of a six-plate coupler.

Designator	Description	Values
$l_1$	Plate length	300 mm
$l_2$	Plate length	600 mm
$l_{s1}$	Plate separation	400 mm
$l_{s2}$	Plate separation	100 mm
$l_{e1}, l_{e2}$	Plate shielding edge	200 mm
$l_{e3}, l_{e4}$	Plate shielding edge	50 mm
$d_{12}$	Transferred distance	100 mm
$d_1$	Shielding distance	50 mm
$d_2$	Shielding distance	20 mm
$t_p$	Plate thickness	2 mm

In order to obtain the appropriate plate length  $l_1$  and shielding distance  $d_1$ , ANSYS Maxwell was used to simulate the coupling capacitors under different  $l_1$  and  $d_1$  values. According to Equation (24), the optimization objective under different values of  $l_1$  and  $d_1$  can then be obtained. The results are shown in Figure 8, where the ratio values decrease with increasing plate length  $l_1$  and airgap distance  $d_1$ . Without a loss of generality, the plate length was set to 300 mm in this study in order to form an asymmetric capacitive coupler. With the defined  $l_1$ , the plate separation  $l_{s2}$  and the shielding edges  $l_{e1}$  and  $l_{e2}$  could be obtained.

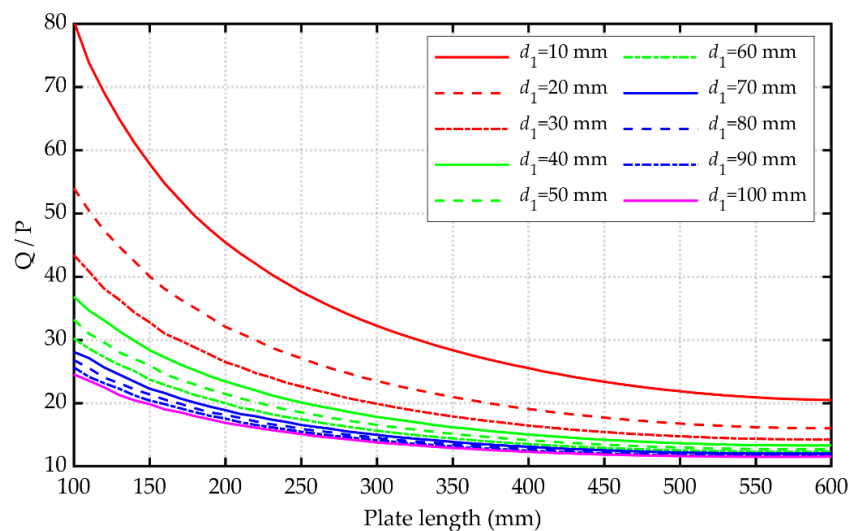
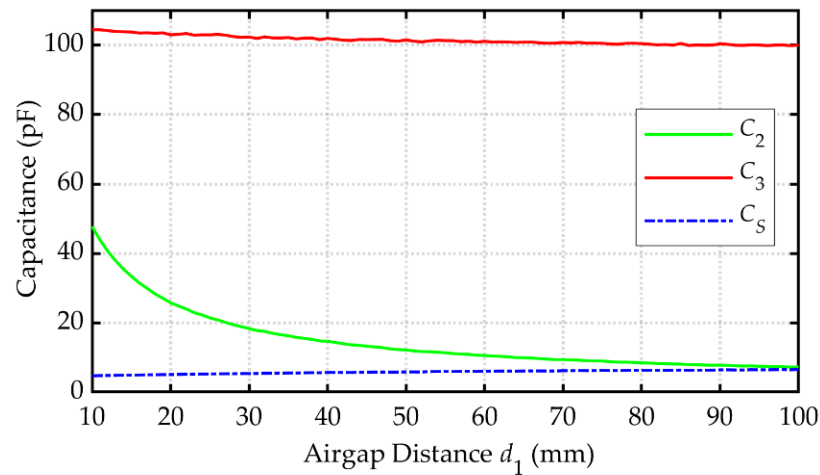


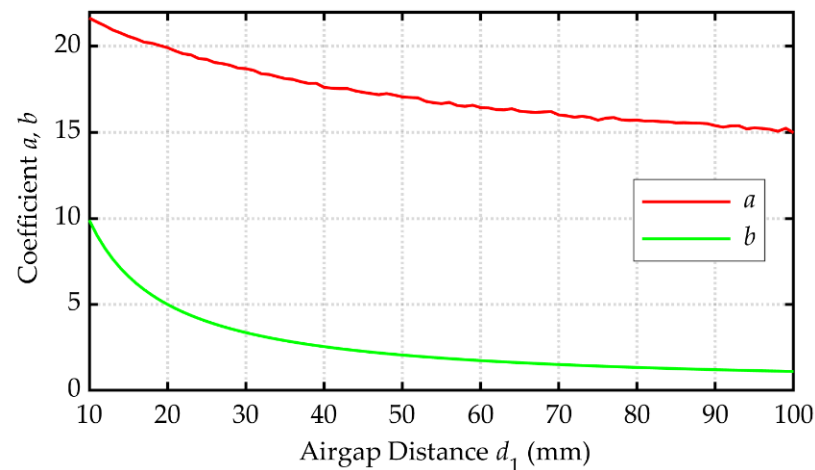
Figure 8. Optimization objective values under different plate length  $l_1$  and airgap distance  $d_1$ .

The only parameter that needed to be seriously considered was the gap distance  $d_1$ . When other parameters are determined, the variation of  $d_1$  can affect the values of the coupling capacitances, which can be simulated by using ANSYS Maxwell. Figure 9 shows the simulated values of  $C_2$ ,  $C_3$ , and  $C_5$  and coefficients  $a$  and  $b$  under different values of airgap distance  $d_1$ .

We can see from Figure 9a that the capacitance of  $C_3$  is greater than that of  $C_2$  and  $C_5$ . With an increasing airgap distance  $d_1$ , the values of  $C_2$  and  $C_3$  decrease, while  $C_5$  increases slightly. As a result, both  $a$  and  $b$  decrease with increasing  $d_1$ , as shown in Figure 9b. In Figure 10, the optimization objective under different distance  $d_1$  is calculated. To reduce the value of  $Q_L/P$ , the value of the gap distance  $d_1$  tends to be large. However, with a large  $d_1$ , the value of  $C_2$  is very small, which enlarges the inductance values and makes the CPT system more sensitive to surrounding disturbances. Therefore, both  $Q_L/P$  and  $C_2$  should be considered in the selection of  $d_1$ . To achieve an appropriate  $Q_L/P$  and avoid  $C_2$  being too small,  $d_1$  was set to 50 mm. Correspondingly,  $Q_L/P$  was set to 16.5,  $a$  was set to 2.06,  $b$  was set to 17.06,  $C_2$  was set to 12.25 pF,  $C_3$  was set to 101.5 pF, and  $C_5$  was set to 5.95 pF.



(a)



(b)

**Figure 9.** Simulated capacitance and coefficients  $a$  and  $b$  under different airgap distance  $d_1$ . (a) Capacitance  $C_2$ ,  $C_3$ , and  $C_5$ . (b) Coefficients  $a$  and  $b$ .

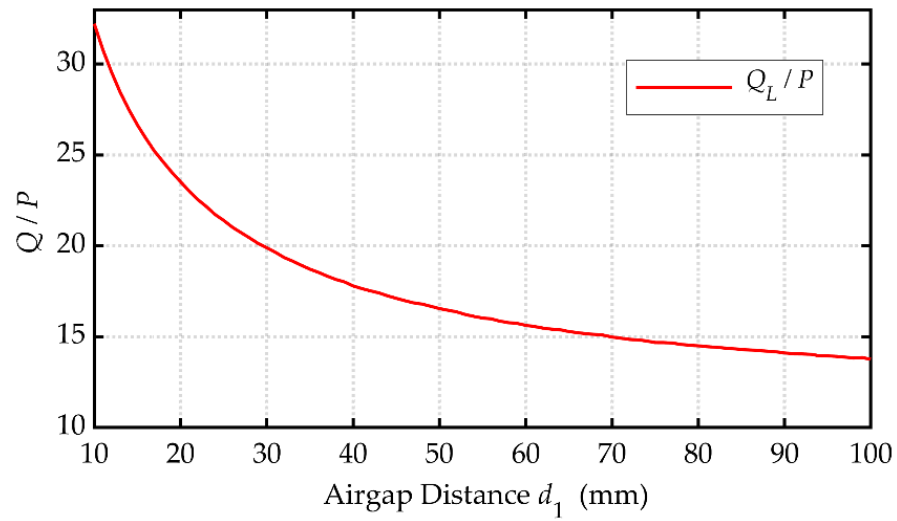


Figure 10. Ratio of reactive power  $Q$  to transferred power under different airgap distance  $d_1$ .

It should be noted that when  $b$  is given, the theoretical minimum  $Q_L/P$  can be obtained from Equations (29) and (30). If we assume that the value of  $b$  does not change with the variation of  $a$ , the relationship between the ratio of  $Q_L/P$  and the coefficient  $a$  is shown in Figure 11. The minimum  $Q_L/P$  value of 10 can be achieved when the coefficient  $a$  is  $-0.65$ . To make the coefficient  $a$  higher than 0, the value of  $b$  should be less than 5.25.

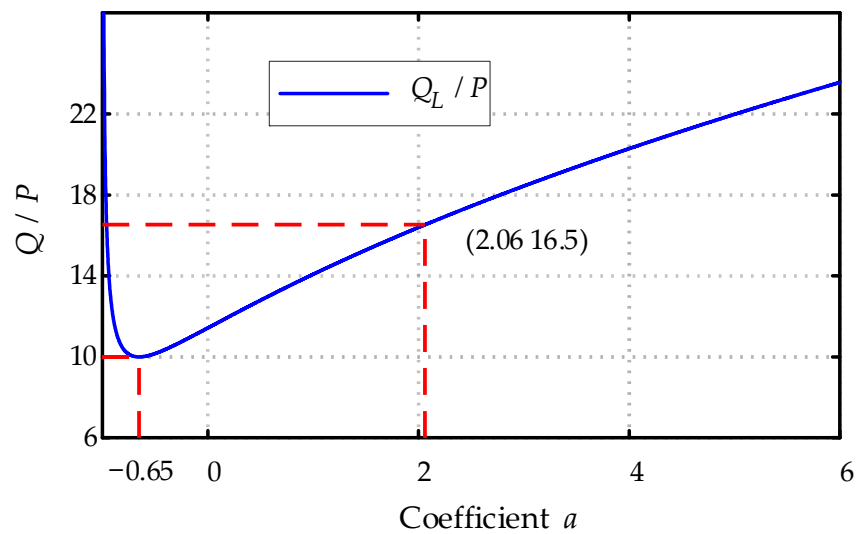
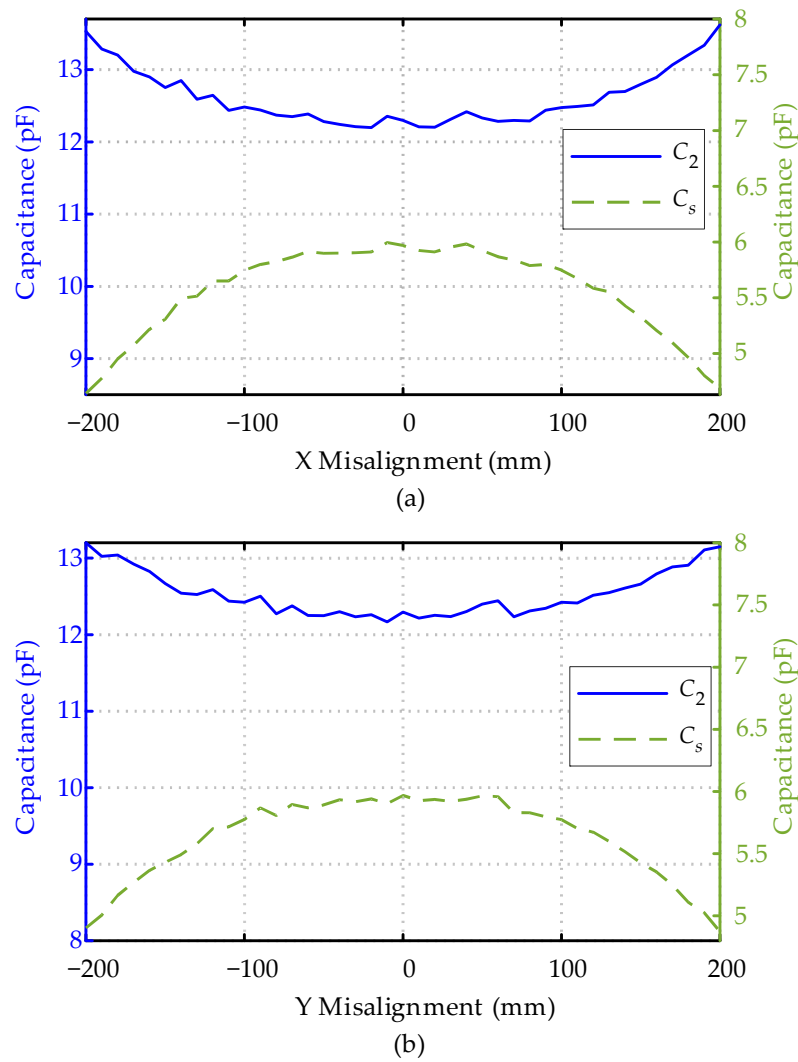


Figure 11. Values of  $Q_L/P$  under different coefficient  $a$ .

Via the finite element simulation software ANSYS Maxwell, the performance of the capacitive coupler with the given parameters was simulated. Figure 12 shows the simulated capacitances  $C_2$  and  $C_5$  under different X and Y misalignments. With an increasing misalignment condition, the simulated  $C_2$  values increase while the  $C_5$  values decrease.



**Figure 12.** Simulated capacitances under X and Y misalignment conditions. (a) Misalignment along x-axis. (b) Misalignment along y-axis.

4.3. Resonant Parameter Design

With the given system parameters, the other resonant parameters can then be obtained. Considering the power losses in an actual system, the transferred power that is used to calculate the circuit parameters should be set slightly higher than the rated value. Based on Equations (6) and (31), the capacitances  $C_1$  and  $C_4$  can be calculated as.

$$\begin{cases} C_1 = \frac{PK_{12}K_{34}\sqrt{(a+1)(b+1)}}{\omega_0 U_{AB}^2} = \frac{3400 \cdot 0.4 \cdot 0.4 \cdot \sqrt{(2.06+1) \cdot (17.06+1)}}{2\pi \cdot 10^6 \cdot 450 \cdot 450 \cdot 8 / \pi^2} = 3.92 \text{ nF} \\ C_4 = \frac{PK_{12}K_{34}\sqrt{(a+1)(b+1)}}{\omega_0 U_{ab}^2} = \frac{3400 \cdot 0.4 \cdot 0.4 \cdot \sqrt{(2.06+1) \cdot (17.06+1)}}{2\pi \cdot 10^6 \cdot 450 \cdot 450 \cdot 8 / \pi^2} = 3.92 \text{ nF} \end{cases} \quad (33)$$

The resonant inductors  $L_1$ ,  $L_2$ ,  $L_3$ , and  $L_4$  can be obtained based on the following resonant relationship:

$$\omega_0 = 2\pi f = 1/\sqrt{L_1 C_1} = 1/\sqrt{L_4 C_4} = 1/\sqrt{L_2 \cdot \left(C_2 + \frac{C_3 C_5}{C_3 + C_5}\right)} = 1/\sqrt{L_3 \cdot \left(C_3 + \frac{C_2 C_5}{C_2 + C_5}\right)} \quad (34)$$

The designed system’s parameters are shown in Table 3. It should be noted that the parasitic capacitance between the windings of the inductors is inevitable and should not be eliminated in this study. The structure of the actual inductor is shown in Figure 13.

Generally, the parallel-connected parasitic capacitance in the inductors is very small (usually in the range of several picofarads), which is close to the capacitance values of  $C_2$  and  $C_5$ . As a result, the resonant inductors  $L_2$  and  $L_3$  deviated from the design values. Besides this, the metal plates were deformed due to the influence of gravity, resulting in a small variation of the coupling capacitance  $C_5$ . Considering the actual value of the ceramic capacitors and the effect of parasitic capacitances in the inductors,  $C_1$  and  $C_4$  were adjusted to 4.2 nF. To avoid measurement errors, the parameters were tuned by using a network analyzer.

**Table 3.** Circuit parameters in the designed CPT system.

Designator	Description	Calculated Values	Actual Values
$L_1$	Input side inductor	6.46 $\mu\text{H}$	5.7 $\mu\text{H}$
$L_2$	Primary side inductor (parallel-connected parasitic capacitor)	1.41 mH	883 $\mu\text{H}$ 9.5 pF
$L_3$	Secondary side inductor (parallel-connected parasitic capacitor)	240.1 $\mu\text{H}$	209 $\mu\text{H}$ 14.5 pF
$L_4$	Output side inductor	6.46 $\mu\text{H}$	5.7 $\mu\text{H}$
$C_1$	Input side capacitor	3.92 nF	4.2 nF
$C_2$	Primary side capacitor	12.25 pF	12.25 pF
$C_3$	Secondary side capacitor	101.5 pF	101.5 pF
$C_4$	Output side capacitor	3.92 nF	4.2 nF
$C_5$	Coupling capacitor	5.95 pF	6.75 pF

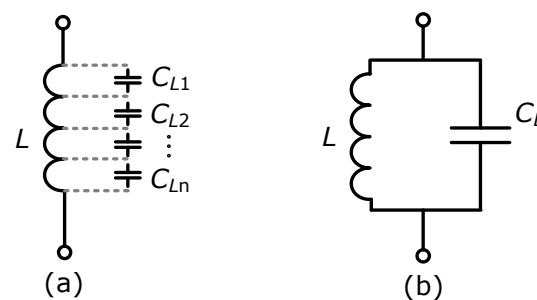


**Figure 13.** Circuit model of actual inductor. (a) Equivalent circuit. (b) Simplified circuit.

## 5. Simulation and Experimental Results

### 5.1. Simulation Results

In this study, the system's performance was simulated by using LTspice. The circuit that is shown in Figure 4 was used to model the proposed CPT system. The simulation's results are shown in Figures 14–16. The waveforms of the voltages  $U_{C2}$  and  $U_{C3}$ , input current, and voltage ( $I_1$  and  $U_{AB}$ ) are shown in Figure 14. Due to the asymmetric configuration of the CPT system, the rms values of  $U_{C2}$  are greater than those of  $U_{C3}$ . The phase difference between  $U_{C2}$  and  $U_{C3}$  is about  $78^\circ$ . The phases of the current and voltage on the input side are almost identical, which allowed the system to operate at high-power factor conditions.

The simulated values of  $Q_L$  and  $Q_L/P$  under different values of the coefficient  $a$  are shown in Figure 15. The results show that the reactive power increases with increasing output power and coefficient  $a$  value and the ratio of  $Q_L/P$  increases with increasing coefficient  $a$  value and decreases with increasing output power. In this study, the coefficient  $a$  was set to 2, and the value of  $Q_L/P$  at the rated power was approximately 17, which agrees well with the designed value.

The system efficiency under different values of the coefficient  $a$  was simulated and the results are displayed in Figure 16. The results show that the system efficiency increased with increasing output power and it decreased with increasing values of the coefficient  $a$ . The trend of system efficiency in Figure 15 is opposite to that of  $Q_L/P$  in Figure 15, which agrees well with the analysis.

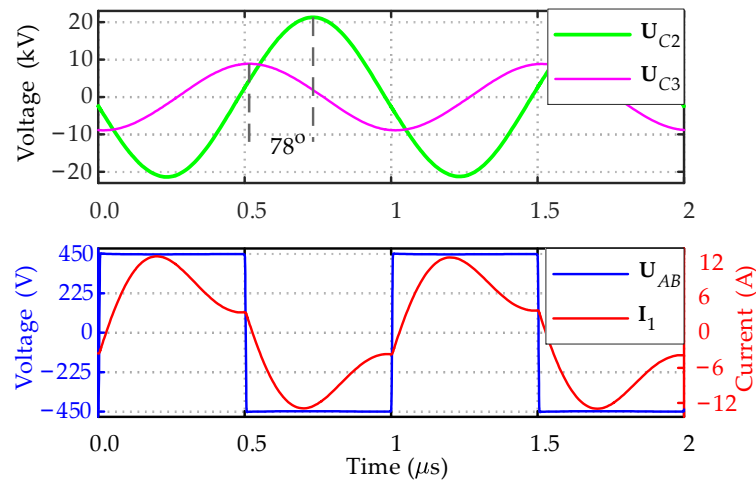


Figure 14. Simulation of  $U_{C2}$ ,  $U_{C3}$ ,  $U_{AB}$ , and  $I_1$ .

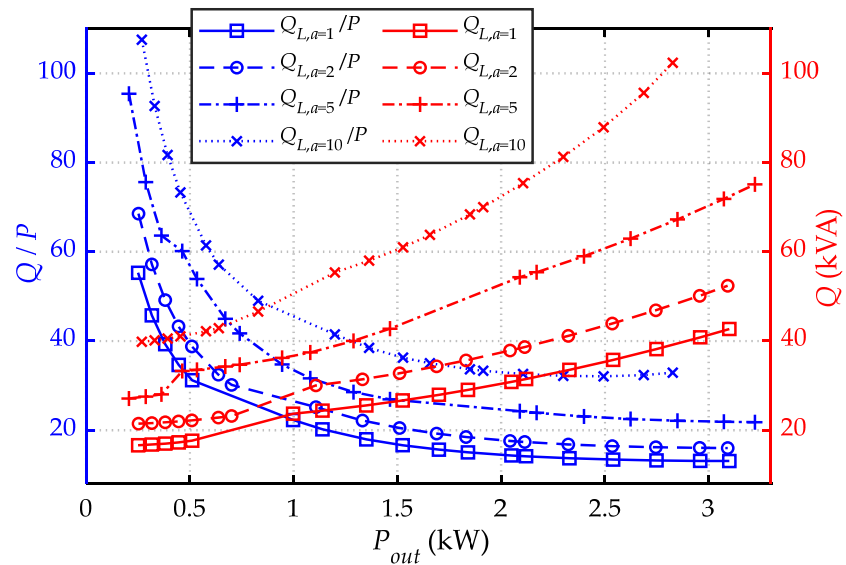


Figure 15. The simulated  $Q$  and  $Q/P$  at different output power  $P_{out}$ .

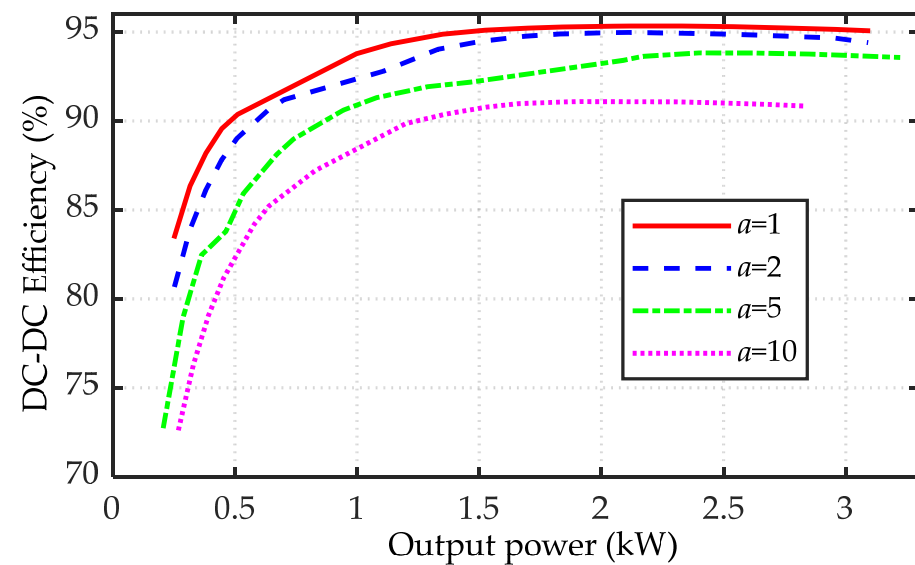


Figure 16. System efficiency at different output power.

The voltages between the plates in the CPT system with different values of coefficient  $a$  were also analyzed. By using the proposed method, the system parameters under different values of  $a$  can be obtained. The voltages between the plates at the rated power can then be calculated as shown in Table 4. The voltages between the shielding plates ( $P_5$  and  $P_6$ ) were almost 0, which shows a good shielding effect in this design. Since the circuit parameters in designed CPT system were asymmetric, the voltages between the plates in the primary and secondary side were different. The voltages between the transmitting plates ( $P_1$  and  $P_2$ ) were higher than those which were observed between the receiving plates ( $P_3$  and  $P_4$ ). When the value of  $a$  increased from 1 to 10, the voltages between the plates in the transmitting side ( $P_1$ ,  $P_2$ , and  $P_5$ ) decreased, while in the receiving side ( $P_3$ ,  $P_4$ , and  $P_6$ ) the voltages increased. Besides this, the voltages between the transmission plates ( $P_1$  and  $P_3$ ) decreased with the increasing value of  $a$ . In this study, the voltage between  $P_1$  and  $P_5$  was approximately 7.56 kV. There was no risk of arcing [48] because the airgap distance between the plates was large.

**Table 4.** Values of the voltages between plates at different  $a$  values.

Parameter	$a = 1$	This Study $a = 2$	$a = 5$	$a = 10$
$ V_{P1-P2} $	15.56 kV	15.14 kV	14.10 kV	12.77 kV
$ V_{P1-P3} $	9.10 kV	8.91 kV	8.56 kV	8.22 kV
$ V_{P3-P4} $	5.53 kV	6.23 kV	7.55 kV	8.86 kV
$ V_{P1-P5} $	7.77 kV	7.56 kV	7.04 kV	6.38 kV
$ V_{P3-P6} $	2.76 kV	3.12 kV	3.77 kV	4.43 kV
$ V_{P5-P6} $	0	0	0	0

## 5.2. Experimental Verification

To verify the proposed method, a 3.2-kW CPT prototype was built as shown in Figure 17. The asymmetric capacitive coupler with a large receiver and small transmitter was made up of six aluminum plates. The plates were held by PVC tubes and ceramic insulators and the outside shielding plates were floating. Under the capacitive coupler, a black steel plate was used as the ground. The mutual capacitance was 6.75 pF and the transferred distance was 100 mm. Just like the schematic circuit that is shown in Figure 4, a DC power source was used in order to provide a DC voltage to the inverter on the transmitting side of this prototype. An electric DC load, together with several parallel-connected resistors, was used as the load and connected to the rectifier on the receiving side. The power converters were formed by SiC devices IMZ120R045M1 and IDW40G120C5B. The inductors  $L_1$ – $L_4$  were wound onto the PVC tubes with 1200-strand Litz wire with a diameter of 0.04 mm, which allowed easy adjustment of the coupling coefficients  $K_{12}$  and  $K_{34}$ . The compensation capacitors consisted of high voltage, low dissipation factor ceramic capacitors.

From the designed prototype, the experimental results at the rated power are shown in Figures 18 and 19. The plates in the coupler were well aligned. In order to reduce the switching losses and improve the system's efficiency, zero-voltage turn-on should be achieved for the switching devices. By slightly reducing the value of inductor  $L_2$ , the ZVS condition was realized, as shown in Figure 18a,b. The waveforms of the input voltage and current were almost in phase and the ZVS condition was achieved by a phase shift of the input current. At the rated input and output DC voltages, about 3.2 kW power was delivered from the DC source to the electric DC load and resistors with an efficiency of 95%. The transmission efficiency under different output power is shown in the Figure 19. With different output voltages, the maximum system efficiencies were both higher than 94.5%.

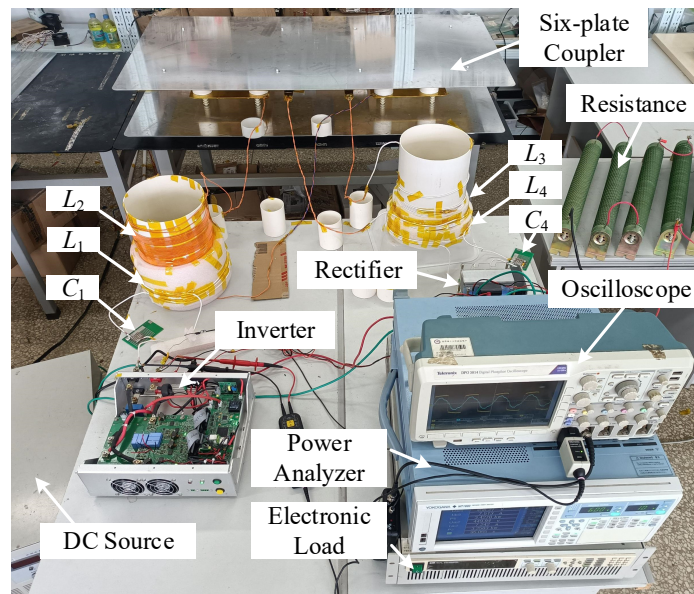
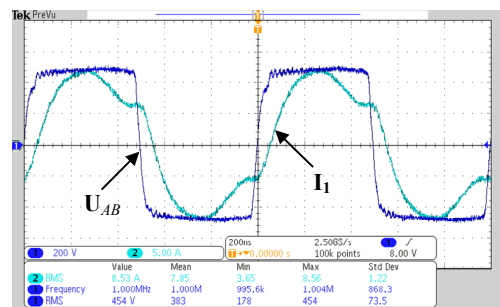
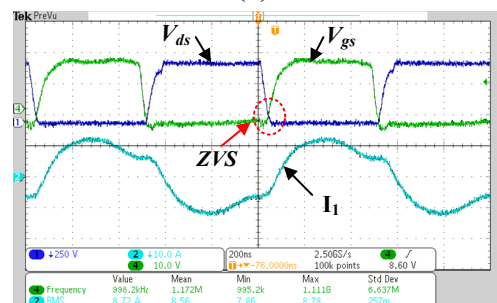


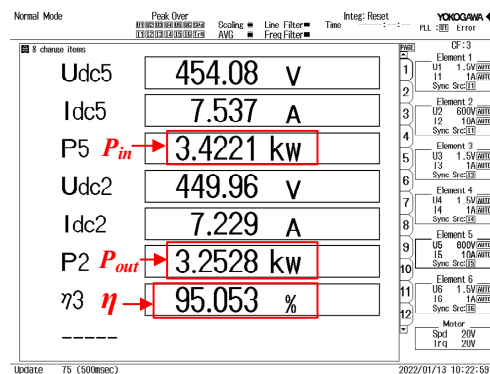
Figure 17. Configuration of a 3.2-kW CPT prototype.



(a)



(b)



(c)

Figure 18. Experimental Results. (a) Experimental  $U_{AB}$  and  $I_1$ . (b) ZVS condition. (c) System efficiency.

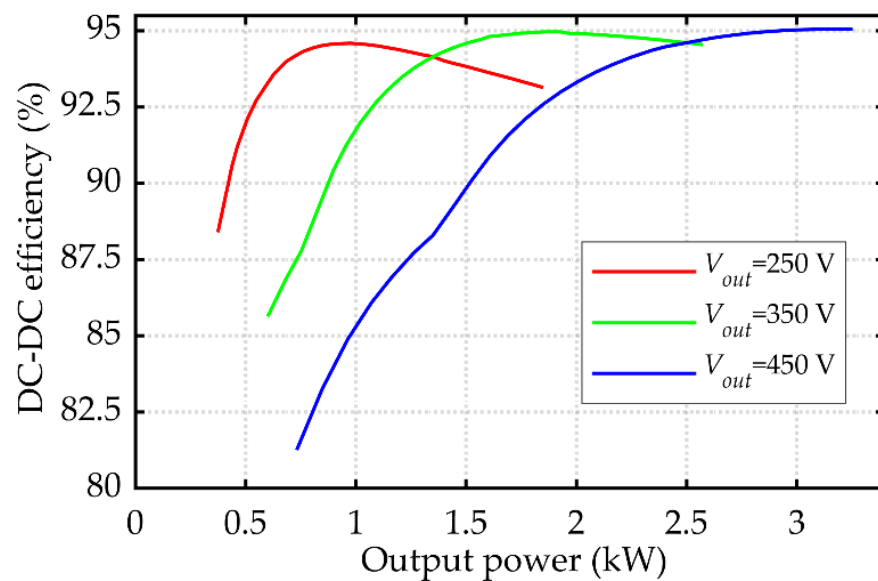


Figure 19. Experimental DC–DC efficiency at different output power.

The comparison between the presently designed CPT system and the previous published CPT systems that have a large airgap distance and kilowatt-scale power is shown in Table 5. The DC–DC overall efficiency is considered. As shown in Table 5, the airgap and coupling area that were used in this study are small, resulting in a lower volume and coupling capacitance. When the element numbers of the systems are similar, the designed CPT system can achieve high transmission efficiency with a relatively low coupling capacitance.

Table 5. Comparison of related CPT system.

Reference	Power [kW]	Efficiency (DC–DC) [%]	Frequency [MHz]	Distance [mm]	Plate area [cm <sup>2</sup> ]	Capacitor $C_S$ [pF]	Elements Num.
[25]	2.4	90.8	1	150	7442	18.35	9
[44]	1.88	85.87	1	150	7442	11.3	9
[48]	1.97	91.65	1	150	7442	9.91	9
[40]	1.5	93.57	1	150	7442	12.8	9
[50]	3.0	95.7	1	100	7200	16.33	7
This study	3.2	95	1	100	1800	6.75	7

The power loss distribution of the presently designed system was analyzed. According to the calculation method that was proposed in [44,63,64], the power losses in the MOSFETs, diodes, inductors, and capacitors were obtained. Based on the on-resistance and switching-off current, the losses in the switching devices could then be calculated; the losses in the inductors and capacitors were obtained from the measured quality factors. The remaining losses are from within the coupling plates. As shown in Figure 20, the inductors and capacitive coupler dissipate 39.2% and 33.6% of the total loss, respectively, which makes up the main losses of the system.

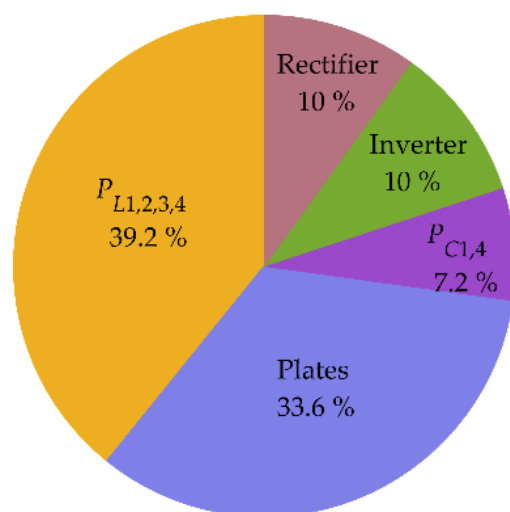


**Figure 20.** The estimated power loss distribution.

## 6. Conclusions

A general parameter optimization method for an asymmetric CPT system is proposed in this article. A six-plate capacitive coupler with an asymmetric structure was used and compensated by an EFR compensation circuit. The asymmetric coupler structure was analyzed and the whole system was modeled. The relationship between the transferred power and reactive power was analyzed. Based on the properties of a linear CPT system, an optimization method was proposed. By using the equal reactive power, the circuit conditions that are required in order to optimize the reactive power were obtained. With these circuit conditions, the reactive power was simplified and the circuit parameters were optimized. Based on the optimization process, a general parameter optimization method was proposed and implemented on a 3.2-kW, 1 MHz CPT prototype. Both the simulated and experimental results show that, with the proposed method, high system efficiency can be achieved for an asymmetric CPT system with low coupling capacitance. About 3.2 kW of power was transferred with a DC–DC efficiency of 95%. Although the special compensation topology and an asymmetric coupler were used in this study, the proposed method is not limited to this topology and it is suitable for both symmetric and asymmetric CPT systems.

**Author Contributions:** Article outline, X.Y. and S.L. (Siqi Li), conceptualization and methodology, J.X., X.Y. and S.L. (Siqi Li); investigation, J.X., W.D. and T.L.; formal analysis and writing—original draft preparation, J.X.; writing—review and editing, S.L. (Sizhao Lu), X.Y. and J.L. All authors have read and agreed to the published version of the manuscript.

**Funding:** This work was supported in part by the National Natural Science Foundation of China under Grant 51607081 and in part by the National Key Research and Development Plan under Grant 2017YFB0103203.

**Conflicts of Interest:** The authors declare no conflict of interest.

## Appendix A

The conditions under which CPT systems have different quality factors are analyzed in Appendix A. According to the analysis that was presented in Section 2.4, when other parameters are determined, the transmission efficiency of the CPT system is dependent on the reactive power and quality factors of the circuit components. With unequal quality

factors applied on the circuit components, the optimization objective expression in the study can then be changed to

$$\sum \frac{Q_{Lj}}{Q_{Lj}^*P} + \sum \frac{Q_{Ci}}{Q_{Ci}^*P} \quad (j = 1, 2, 3, 4; i = S, 1, 2, 3, 4). \quad (\text{A1})$$

When a CPT system is built, the quality factors of the circuit components are determined. Here, the quality factors can be seen as independent from each other. Since the quality factors do not affect the independence of the system parameters, the properties of linear CPT system can also be used to reduce the complexity of the optimization objective. The difference is that, with unequal quality factors, the circuit conditions that are obtained to simplify the optimization objective contain unequal quality factors.

The parameter optimization design process for a CPT system with unequal quality factors is similar to that of one with equal quality factors. Therefore, we just demonstrate the optimization of a CPT system with equal quality factors in this article.

## References

1. Yang, Y.; El Baghdadi, M.; Lan, Y.; Benomar, Y.; Van Mierlo, J.; Hegazy, O. Design Methodology, Modeling, and Comparative Study of Wireless Power Transfer Systems for Electric Vehicles. *Energies* **2018**, *11*, 1716. [[CrossRef](#)]
2. Rahmani, F.; Niknejad, P.; Agarwal, T.; Barzegaran, M. Gallium Nitride Inverter Design with Compatible Snubber Circuits for Implementing Wireless Charging of Electric Vehicle Batteries. *Machines* **2020**, *8*, 56. [[CrossRef](#)]
3. Li, S.; Lu, S.; Mi, C.C. Revolution of Electric Vehicle Charging Technologies Accelerated by Wide Bandgap Devices. *Proc. IEEE* **2021**, *109*, 985–1003. [[CrossRef](#)]
4. Dai, J.; Ludois, D.C. A Survey of Wireless Power Transfer and a Critical Comparison of Inductive and Capacitive Coupling for Small Gap Applications. *IEEE Trans. Power Electron.* **2015**, *30*, 6017–6029. [[CrossRef](#)]
5. Lu, F.; Zhang, H.; Mi, C. A Review on the Recent Development of Capacitive Wireless Power Transfer Technology. *Energies* **2017**, *10*, 1752. [[CrossRef](#)]
6. Li, S.; Mi, C.C. Wireless Power Transfer for Electric Vehicle Applications. *IEEE J. Emerg. Sel. Top. Power Electron.* **2014**, *3*, 4–17.
7. Zhang, Z.; Pang, H.; Georgiadis, A.; Cecati, C. Wireless Power Transfer—An Overview. *IEEE Trans. Ind. Electron.* **2019**, *66*, 1044–1058. [[CrossRef](#)]
8. Nguyen, V.T.; Kang, S.H.; Choi, J.H.; Jung, C.W. Magnetic Resonance Wireless Power Transfer Using Three-Coil System with Single Planar Receiver for Laptop Applications. *IEEE Trans. Consumer Electron.* **2015**, *61*, 160–166. [[CrossRef](#)]
9. Madhja, A.; Nikolettseas, S.; Voudouris, A.A. Adaptive Wireless Power Transfer in Mobile Ad Hoc Networks. *Comput. Netw.* **2019**, *152*, 87–97. [[CrossRef](#)]
10. Hu, A.P.; Liu, C.; Li, H.L. A Novel Contactless Battery Charging System for Soccer Playing Robot. In Proceedings of the 2008 15th International Conference on Mechatronics and Machine Vision in Practice, Auckland, New Zealand, 2–4 December 2008; pp. 646–650.
11. Culurciello, E.; Andreou, A.G. Capacitive Inter-Chip Data and Power Transfer for 3-D VLSI. *IEEE Trans. Circuits Syst. II Express Briefs* **2006**, *53*, 1348–1352. [[CrossRef](#)]
12. Jiang, C.; Chau, K.T.; Ching, T.W.; Liu, C.; Han, W. Time-Division Multiplexing Wireless Power Transfer for Separately Excited DC Motor Drives. *IEEE Trans. Magn.* **2017**, *53*, 1–5. [[CrossRef](#)]
13. Raval, P.; Kacprzak, D.; Hu, A.P. A Multi-Phase 3D Inductive Power Transfer System Based on a Rotating Magnetic Field. *IEEE Trans. Ind. Electron.* **2015**, *62*, 795–802. [[CrossRef](#)]
14. Ludois, D.C.; Reed, J.K.; Hanson, K. Capacitive Power Transfer for Rotor Field Current in Synchronous Machines. *IEEE Trans. Power Electron.* **2012**, *27*, 4638–4645. [[CrossRef](#)]
15. Zhou, Y.; Liu, C.; Huang, Y. Wireless Power Transfer for Implanted Medical Application: A Review. *Energies* **2020**, *13*, 2837. [[CrossRef](#)]
16. Li, L.; Liu, H.; Zhang, H.; Xue, W. Efficient Wireless Power Transfer System Integrating with Metasurface for Biological Applications. *IEEE Trans. Ind. Electron.* **2018**, *65*, 3230–3239. [[CrossRef](#)]
17. Hu, A.P.; You, Y.W.; Chen, F.-Y.B.; McCormick, D.; Budgett, D.M. Wireless Power Supply for ICP Devices with Hybrid Supercapacitor and Battery Storage. *IEEE J. Emerg. Sel. Top. Power Electron.* **2016**, *4*, 273–279. [[CrossRef](#)]
18. Palagani, Y.; Mohanarangam, K.; Shim, J.H.; Choi, J.R. Wireless Power Transfer Analysis of Circular and Spherical Coils under Misalignment Conditions for Biomedical Implants. *Biosens. Bioelectron.* **2019**, *141*, 111283. [[CrossRef](#)]
19. Sodagar, A.M.; Amiri, P. Capacitive Coupling for Power and Data Telemetry to Implantable Biomedical Microsystems. In Proceedings of the 2009 4th International IEEE/EMBS Conference on Neural Engineering, Antalya, Turkey, 29 April–2 May 2009; pp. 411–414.
20. Deng, J.; Pang, B.; Shi, W.; Wang, Z. A New Integration Method with Minimized Extra Coupling Effects Using Inductor and Capacitor Series-Parallel Compensation for Wireless EV Charger. *Appl. Energy* **2017**, *207*, 405–416. [[CrossRef](#)]

21. Zhao, L.; Thrimawithana, D.; Madawala, U.; Hu, A.; Mi, C. A Misalignment-Tolerant Series-Hybrid Wireless EV Charging System with Integrated Magnetics. *IEEE Trans. Power Electron.* **2018**, *34*, 1276–1285. [[CrossRef](#)]
22. Zhou, S.; Chris Mi, C. Multi-Paralleled LCC Reactive Power Compensation Networks and Their Tuning Method for Electric Vehicle Dynamic Wireless Charging. *IEEE Trans. Ind. Electron.* **2016**, *63*, 6546–6556. [[CrossRef](#)]
23. Lu, F. High Power Capacitive Power Transfer for Electric Vehicle Charging Applications. Ph.D. Dissertation, University Michigan, Ann Arbor, MI, USA, 2017.
24. Lu, F.; Zhang, H.; Mi, C. A Two-Plate Capacitive Wireless Power Transfer System for Electric Vehicle Charging Applications. *IEEE Trans. Power Electron.* **2018**, *33*, 964–969. [[CrossRef](#)]
25. Lu, F.; Zhang, H.; Hofmann, H.; Mi, C. A Double-Sided LCLC-Compensated Capacitive Power Transfer System for Electric Vehicle Charging. *IEEE Trans. Power Electron.* **2015**, *30*, 6011–6014. [[CrossRef](#)]
26. Mohamed, A.A.; Shaier, A.A.; Metwally, H.; Selem, S.I. A Comprehensive Overview of Inductive Pad in Electric Vehicles Stationary Charging. *Appl. Energy* **2020**, *262*, 114584. [[CrossRef](#)]
27. Lu, F.; Mi, C.C. An Inductive and Capacitive Combined Wireless Power Transfer System with LC-Compensated Topology. *IEEE Trans. Power Electron.* **2016**, *31*, 12. [[CrossRef](#)]
28. Rituraj, G.; Joy, E.R.; Kushwaha, B.K.; Kumar, P. Analysis and Comparison of Series-Series and Series-Parallel Topology of Contactless Power Transfer Systems. In Proceedings of the TENCON 2014–2014 IEEE Region 10 Conference, Bangkok, Thailand, 22–25 October 2014; pp. 1–6.
29. Zahid, Z.U.; Dalala, Z.M.; Zheng, Z.; Chen, R.; Faraci, W.E.; Lai, J.-S.J.; Lisi, G.; Anderson, D. Modeling and Control of Series-Series Compensated Inductive Power Transfer System. *IEEE J. Emerg. Sel. Top. Power Electron.* **2015**, *3*, 111–123. [[CrossRef](#)]
30. Zhang, W.; Mi, C.C. Compensation Topologies of High-Power Wireless Power Transfer Systems. *IEEE Trans. Veh. Technol.* **2016**, *65*, 4768–4778. [[CrossRef](#)]
31. Li, S.; Li, W.; Deng, J.; Nguyen, T.D.; Mi, C.C. A Double-Sided LCC Compensation Network and Its Tuning Method for Wireless Power Transfer. *IEEE Trans. Veh. Technol.* **2015**, *64*, 2261–2273. [[CrossRef](#)]
32. Lu, F.; Zhang, H.; Hofmann, H.; Su, W.; Mi, C.C. A Dual-Coupled LCC-Compensated IPT System with a Compact Magnetic Coupler. *IEEE Trans. Power Electron.* **2018**, *33*, 6391–6402. [[CrossRef](#)]
33. Hou, J.; Chen, Q.; Zhang, Z.; Wong, S.-C.; Tse, C.K. Analysis of Output Current Characteristics for Higher Order Primary Compensation in Inductive Power Transfer Systems. *IEEE Trans. Power Electron.* **2018**, *33*, 6807–6821. [[CrossRef](#)]
34. Hou, J.; Chen, Q.; Wong, S.-C.; Tse, C.K.; Ruan, X. Analysis and Control of Series/Series-Parallel Compensated Resonant Converter for Contactless Power Transfer. *IEEE J. Emerg. Sel. Top. Power Electron.* **2015**, *3*, 124–136. [[CrossRef](#)]
35. Hou, J.; Chen, Q.; Ren, X.; Ruan, X.; Wong, S.-C.; Tse, C.K. Precise Characteristics Analysis of Series/Series-Parallel Compensated Contactless Resonant Converter. *IEEE J. Emerg. Sel. Top. Power Electron.* **2015**, *3*, 101–110. [[CrossRef](#)]
36. Villa, J.L.; Sallan, J.; Sanz Osorio, J.F.; Llombart, A. High-Misalignment Tolerant Compensation Topology For ICPT Systems. *IEEE Trans. Ind. Electron.* **2012**, *59*, 945–951. [[CrossRef](#)]
37. Lu, J.; Zhu, G.; Lin, D.; Zhang, Y.; Wang, H.; Mi, C.C. Realizing Constant Current and Constant Voltage Outputs and Input Zero Phase Angle of Wireless Power Transfer Systems with Minimum Component Counts. *IEEE Trans. Intell. Transp. Syst.* **2021**, *22*, 600–610. [[CrossRef](#)]
38. Qu, X.; Jing, Y.; Han, H.; Wong, S.-C.; Tse, C.K. Higher Order Compensation for Inductive-Power-Transfer Converters with Constant-Voltage or Constant-Current Output Combating Transformer Parameter Constraints. *IEEE Trans. Power Electron.* **2017**, *32*, 394–405. [[CrossRef](#)]
39. Qin, R.; Li, J.; Costinett, D. A 6.6-KW High Frequency Wireless Power Transfer System for Electric Vehicle Charging Using Multi-Layer Non-Uniform Self-Resonant Coil at MHz. *IEEE Trans. Power Electron.* **2021**, *37*, 4842–4856. [[CrossRef](#)]
40. Li, L.; Wang, Z.; Gao, F.; Wang, S.; Deng, J. A Family of Compensation Topologies for Capacitive Power Transfer Converters for Wireless Electric Vehicle Charger. *Appl. Energy* **2020**, *260*, 114156. [[CrossRef](#)]
41. Zou, Y.; Zhu, J.; Wang, X.; Hanzo, L. A Survey on Wireless Security: Technical Challenges, Recent Advances, and Future Trends. *Proc. IEEE* **2016**, *104*, 1727–1765. [[CrossRef](#)]
42. Ludois, D.C.; Erickson, M.J.; Reed, J.K. Aerodynamic Fluid Bearings for Translational and Rotating Capacitors in Noncontact Capacitive Power Transfer Systems. *IEEE Trans. Ind. Appl.* **2014**, *50*, 1025–1033. [[CrossRef](#)]
43. Zhu, Q.; Zou, L.J.; Su, M.; Hu, A.P. Four-Plate Capacitive Power Transfer System with Different Grounding Connections. *Int. J. Electr. Power Energy Syst.* **2020**, *115*, 105494. [[CrossRef](#)]
44. Zhang, H.; Lu, F.; Hofmann, H.; Liu, W.; Mi, C.C. A Four-Plate Compact Capacitive Coupler Design and LCL-Compensated Topology for Capacitive Power Transfer in Electric Vehicle Charging Application. *IEEE Trans. Power Electron.* **2016**, *31*, 8541–8551. [[CrossRef](#)]
45. Liu, Y.; Wu, T.; Fu, M. Interleaved Capacitive Coupler for Wireless Power Transfer. *IEEE Trans. Power Electron.* **2021**, *36*, 13526–13535. [[CrossRef](#)]
46. Zhang, H.; Lu, F. An Improved Design Methodology of the Double-Sided LC -Compensated CPT System Considering the Inductance Detuning. *IEEE Trans. Power Electron.* **2019**, *34*, 11396–11406. [[CrossRef](#)]
47. Wang, Y.; Zhang, H.; Lu, F. Capacitive Power Transfer with Series-Parallel Compensation for Step-Up Voltage Output. *IEEE Trans. Ind. Electron.* **2021**, *69*, 5604–5614. [[CrossRef](#)]

48. Zhang, H.; Lu, F.; Hofmann, H.; Liu, W.; Mi, C.C. Six-Plate Capacitive Coupler to Reduce Electric Field Emission in Large Air-Gap Capacitive Power Transfer. *IEEE Trans. Power Electron.* **2018**, *33*, 665–675. [[CrossRef](#)]
49. Li, S.; Liu, Z.; Zhao, H.; Zhu, L.; Shuai, C.; Chen, Z. Wireless Power Transfer by Electric Field Resonance and Its Application in Dynamic Charging. *IEEE Trans. Ind. Electron.* **2016**, *63*, 6602–6612. [[CrossRef](#)]
50. Xia, J.; Yuan, X.; Lu, S.; Li, J.; Luo, S.; Li, S. A Two-Stage Parameter Optimization Method for Capacitive Power Transfer Systems. *IEEE Trans. Power Electron.* **2022**, *37*, 1102–1117. [[CrossRef](#)]
51. Lu, F.; Zhang, H.; Hofmann, H.; Mi, C. A CLLC-Compensated High Power and Large Air-Gap Capacitive Power Transfer System for Electric Vehicle Charging Applications. In Proceedings of the 2016 IEEE Applied Power Electronics Conference and Exposition (APEC), IEEE, Long Beach, CA, USA, 20–24 March 2016; pp. 1721–1725.
52. Sinha, S.; Kumar, A.; Afridi, K.K. Improved Design Optimization of Efficient Matching Networks for Capacitive Wireless Power Transfer Systems. In Proceedings of the 2018 IEEE Applied Power Electronics Conference and Exposition (APEC), San Antonio, TX, USA, 4–8 March 2018; pp. 3167–3173.
53. Sinha, S.; Kumar, A.; Regensburger, B.; Afridi, K.K. Design of High-Efficiency Matching Networks for Capacitive Wireless Power Transfer Systems. *IEEE J. Emerg. Sel. Top. Power Electron.* **2020**, *10*, 104–127. [[CrossRef](#)]
54. Kumar, A.; Sinha, S.; Sepahvand, A.; Afridi, K.K. Improved Design Optimization Approach for High Efficiency Matching Networks. In Proceedings of the 2016 IEEE Energy Conversion Congress and Exposition (ECCE), Milwaukee, WI, USA, 18–22 September 2016; pp. 1–7.
55. Sinha, S.; Kumar, A.; Pervaiz, S.; Regensburger, B.; Afridi, K.K. Design of Efficient Matching Networks for Capacitive Wireless Power Transfer Systems. In Proceedings of the 2016 IEEE 17th Workshop on Control and Modeling for Power Electronics (COMPEL), Trondheim, Norway, 27–30 June 2016; pp. 1–7.
56. Kumar, A.; Sinha, S.; Sepahvand, A.; Afridi, K.K. Improved Design Optimization for High-Efficiency Matching Networks. *IEEE Trans. Power Electron.* **2018**, *33*, 37–50. [[CrossRef](#)]
57. Kim, T.-H.; Yun, G.-H.; Lee, W.Y.; Yook, J.-G. Asymmetric Coil Structures for Highly Efficient Wireless Power Transfer Systems. *IEEE Trans. Microw. Theory Tech.* **2018**, *66*, 3443–3451. [[CrossRef](#)]
58. Nguyen, M.T.; Nguyen, C.V.; Truong, L.H.; Le, A.M.; Quyen, T.V.; Masaracchia, A.; Teague, K.A. Electromagnetic Field Based WPT Technologies for UAVs: A Comprehensive Survey. *Electronics* **2020**, *9*, 461. [[CrossRef](#)]
59. Cai, C.; Wang, J.; Nie, H.; Zhang, P.; Lin, Z.; Zhou, Y.-G. Effective-Configuration WPT Systems for Drones Charging Area Extension Featuring Quasi-Uniform Magnetic Coupling. *IEEE Trans. Transp. Electrification.* **2020**, *6*, 920–934. [[CrossRef](#)]
60. Zhu, Q.; Zhang, Y.; Liao, C.; Guo, Y.; Wang, L.; Li, F. Experimental Study on Asymmetric Wireless Power Transfer System for Electric Vehicle Considering Ferrous Chassis. *IEEE Trans. Transp. Electrification.* **2017**, *3*, 427–433. [[CrossRef](#)]
61. Moon, S.; Moon, G.-W. Wireless Power Transfer System with an Asymmetric Four-Coil Resonator for Electric Vehicle Battery Chargers. *IEEE Trans. Power Electron.* **2016**, *31*, 6844–6854. [[CrossRef](#)]
62. Luo, S.; Li, S.; Zhao, H. Reactive Power Comparison of Four-Coil, LCC and CLC Compensation Network for Wireless Power Transfer. In Proceedings of the 2017 IEEE PELS Workshop on Emerging Technologies: Wireless Power Transfer (WoW), Chongqing, China, 20–22 May 2017; pp. 268–271.
63. Lu, F.; Zhang, H.; Hofmann, H.; Mi, C. A High Efficiency 3.3 KW Loosely-Coupled Wireless Power Transfer System without Magnetic Material. In Proceedings of the 2015 IEEE Energy Conversion Congress and Exposition (ECCE), Montreal, QC, Canada, 20–24 September 2015; pp. 2282–2286.
64. Vu, V.-B.; Dahidah, M.; Pickert, V.; Phan, V.-T. An Improved LCL-L Compensation Topology for Capacitive Power Transfer in Electric Vehicle Charging. *IEEE Access* **2020**, *8*, 27757–27768. [[CrossRef](#)]